Detailed Variations in Urban Surface Temperatures Exploration Based on Unmanned Aerial Vehicle Thermography

Li Feng, Huihui Tian, Zhi Qiao, Menmen Zhao, and Yanxia Liu

***Abstract*—Determining the land surface temperature (LST) variations in urban surfaces using high spatiotemporal resolution thermal infrared data is necessary for urban microthermal environmental modeling. An unmanned aerial vehicle (UAV) equipped with a thermal infrared imager was used to monitor the high-precision spatiotemporal variation of LSTs for six typical urban surfaces, including water, tree canopy, grass, brick pavement, asphalt pavement, and marble pavement, in the Jiangning district, Nanjing. An estimation of sensible heat release was further conducted to quantitatively describe the fine characteristics of the LSTs of these surfaces. The factors influencing LST were investigated by correlating LSTs with the meteorological factors. The results showed that there were significant differences in LSTs and sensible heat release for six typical urban surfaces in sunny and cloudy days, respectively. On sunny days, the diurnal variations in different surfaces fluctuated substantially, which was not evident on cloudy days. The artificial surfaces always represented as the main source of sensible heat release. Solar radiation and air temperature, among the meteorological factors, were positively correlated with the LSTs of the surfaces. The air humidity was negatively correlated with the LSTs and played a role in cooling the land surface.**

***Index Terms*—Land surface temperature (LST), meticulous variation features, sensible heat flux, unmanned aerial vehicle (UAV) thermal infrared, urban surface.**

I. INTRODUCTION

DUE to the increasing urbanization in China, a series of adverse consequences has been associated with urbanization, such as the loss of environmentally fragile lands, reduced open spaces, and increased air pollution [1]. With further improvements in requirements by the populace for comfort, health and safety, microscale environmental conditions have received increasing attention [2]. Wu proposed that the means of "micro" ideas rather than "macro" was more reasonable for ecological city construction and reconstruction of the city's "microcirculation" [3]. Therefore, from "macro" to "micro" is the research direction for urban environmental problems.

As a core part of microenvironmental research, the urban microthermal environment, including air temperature, air humidity, solar radiation, airflow velocity (wind speed), and other physical environmental conditions, is directly related to human health and work efficiency. Influenced by human factors such as small-scale surface properties and infrastructure configuration patterns, the change in surface properties caused by urban expansion and the influence of the spatial distribution pattern and coverage of urban vegetation on the urban microthermal environment is particularly notable [4]. At present, medium(low) resolution [5]–[7], thermal infrared remote sensing data are used to retrieve large-scale land surface temperatures (LSTs), which can provide the basic information for urban thermal environmental research [8]–[13]. However, for urban microthermal environments, high-precision measurements and simulation methods are essential. High-resolution LST is a key part of the microthermal environment. How to achieve accurate LSTs at the microscale should be addressed with urgency [14]. Due to the limited transit time, image resolution, revisiting cycle, and cloud impacts on remote sensing data, it is difficult to obtain high spatiotemporal resolution LSTs for different surfaces. The emergence of unmanned aerial vehicle (UAV) technology can adequately address these shortcomings to provide possibilities for the refined research of urban microthermal environments [15].

As an emerging field, UAV technology has been widely used in agriculture [16]–[18], forestry [19], [20], topographic mapping [21], disaster monitoring [22], [23], and environmental monitoring [24], [25]. With the advent of light and small [26] thermal infrared cameras, thermal infrared technology combined with UAVs has gradually gained favor with more scholars [27]–[30]. The use of UAVs equipped with thermal infrared imagers is also widely used in agriculture [31]–[35], forestry [36]–[38], fire [39], and thermal environment monitoring [40], [41]. Drones equipped with thermal infrared cameras to obtain forest or crop canopy temperatures have mainly been used to explore the relationship between stomatal conductance and drought stress and canopy temperature. Feng *et al.* applied thermal infrared

Manuscript received June 14, 2019; revised September 26, 2019; accepted November 12, 2019. Date of publication December 2, 2019; date of current version February 12, 2020. This work was supported in part by the National Natural Science Foundation of China under Grant 41771446, in part by the Fundamental Research Funds for the Central Universities under Grant 2018B18414, and in part by the National Key Research and Development Program by Ministry of Science and Technology under Grant 2016YFA0601500. *(Corresponding author: Li Feng.)*

L. Feng, H. Tian, M. Zhao, and Y. Liu are with the School of Geographic Science and Engineering, Hohai University, Nanjing 211100, China (e-mail: fly@hhu.edu.cn; tianhuihui@hhu.edu.cn; zhaomm@hhu.edu.cn; liuyanxia@hhu.edu.cn).

Z. Qiao is with the Key Laboratory of Indoor Air Environment Quality Control, School of Environmental Science and Engineering, Tianjin University, Tianjin 300350, China (e-mail: qiaozhi@tju.edu.cn).

Digital Object Identifier 10.1109/JSTARS.2019.2954852

This work is licensed under a Creative Commons Attribution 4.0 License. For more information, see http://creativecommons.org/licenses/by/4.0/

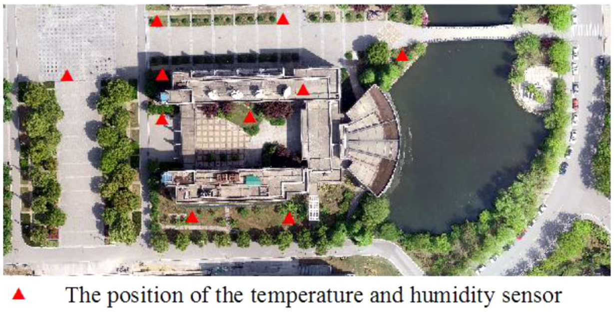

Fig. 1. Orthophoto map of the study area.

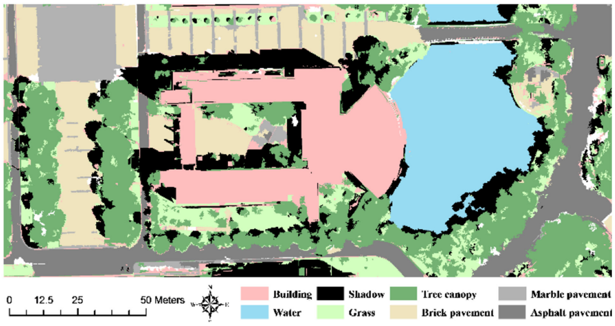

Fig. 2. Surfaces of the study area.

remote sensing technology of UAVs to propose a new coal fire detection method, which improved the accuracy of coal fire identification in mining areas [42]. Dios and Ollero used drones with thermal infrared cameras to monitor the thermal emissions of urban buildings [43]. Webster study three-dimensional thermal characterization of forest canopies using UAV photogrammetry [44]. Wu *et al.* used handheld thermal infrared cameras to obtain thermal infrared image data and analyzed the thermal characteristics of common surface types in typical residential areas [45]. However, there is little literature on the use of UAV thermal infrared technology to conduct research on LST changes and influencing factors of urban surfaces.

Therefore, this study attempted to obtain the variations in LST under different weather conditions for six typical surfaces using a UAV equipped with a thermal infrared camera in a typical area of Nanjing City, and then revealed typical meteorological factors affecting LSTs in the typical surfaces.

II. Study Area and Data

A. Study Area

Nanjing is an important city in the Yangtze River Delta, which is the largest economic zone of China. Nanjing has a humid subtropical climate heavily influenced by the East Asia Monsoon, resulting in a hot rainy summer and cold wet winter, and its thermal environment is complex. This article selected a typical area of a university campus in the Jiangning District of Nanjing as the case study area, as shown in Fig. 1, which includes six common urban surface types. To reveal the detailed features of different thermal cushions in the city, the study area can be further divided into natural surfaces and artificial surfaces. The natural surfaces include water, tree canopy, and grass. The artificial surfaces can be divided into brick pavement, asphalt pavement, and marble pavement, corresponding to different road materials.

B. Data Source

1) Study Area RGB Image and Surface Type Map: To improve the classification accuracy of surface types in the study area, a UAV is equipped with a visible light lens to obtain an RGB image of the study area. The DOM (digital orthophoto map) (see Fig. 1) and classification map (see Fig. 2) of the surface types in the study area can be obtained through data processing.

Fig. 3. UAV and thermal infrared camera.

2) LSTs and Meteorological Data: A UAV equipped with a thermal infrared camera was used to obtain thermal infrared image data of the study area. The UAV is a DJI Phantom which is popular for this application. The DJI Phantom has the advantages of simple operation, high security, and low cost. It can realize intelligent functions such as automatic takeoff, automatic landing, automatic return, high-definition picture return, photography and camera control, and so on. It also makes it easy for novices to master aerial photography skills. The thermal infrared camera is a temperature-sensitive thermal imager for the FLIR Vue Pro 640R drone (see Fig. 3). The specific parameters for the UAV and camera are shown in Table I. The 640R drone temperature measuring camera is a temperature measuring camera designed for small UAVs. It consists mainly of an infrared detector, optical imaging objective, and optical scanning unit. It functions as a temperature gauge and data logger that enables full-width temperature measurement with superimposed outputs of maximum temperature, minimum temperature, and average temperature on thermal imaging video through a front-end processing system. The principle is to detect the thermal infrared radiation information of the target object, convert the thermal infrared radiation energy into an electrical signal, and then process the signal amplification and conversion of the electrical signal, and finally display different temperatures in different colors and convert into thermal infrared images that are recognizable by the human eye. At present, thermal infrared imagers have seen wide use in various studies, and their temperature measurement

TABLE I
PARAMETERS OF THE UAV THERMAL INFRARED CAMERA

Performance parameter	Parameter value
Model of UAV	DJI
Camera model	FLIR Vue Pro 640R
Temperature resolution	0.1℃
Pixel size	17 μm
Wavelength range	7.5 – 13.5 μm
Range of working temperatures	-20℃- 50℃
Temperature measurement accuracy	±2°
Range of temperature measurement	-20℃ - 170℃
Display temperatures	Maximum temperature, Minimum temperature, Average temperature

TABLE II
DATA OBSERVED BY UAV

Data	Weather condition	Observations	Observation interval
2018-4-20	sunny	13	1 h
2018-4-21	cloudy	13	1 h
2018-4-24	cloudy	12	1 h
2018-4-25	sunny	13	1 h
2018-5-27	sunny	13	1 h
2018-6-14	sunny	13	1 h
2018-7-21	sunny	13	1 h
2018-8-25	sunny	13	1 h
2018-9-29	sunny	13	1 h
2018-10-30	sunny	13	1 h
2018-11-25	sunny	13	1 h
2018-12-29	sunny	13	1 h

accuracy has also been confirmed by users [45]. Compared with a traditional hand-held thermal infrared camera for acquisition of LST data, the use of an UAV equipped with a thermal infrared camera to obtain data avoids errors caused by the camera lens and the ground depression angle when photographing.

Since the LST is substantially affected by weather conditions, the LST data of the surface was acquired in different months (April–December) and under different weather conditions (April) in 2018. We obtained 156 LST images in 2018 over a total of 12 days (from 7:00 to 19:00 every day) from April to December under different weather conditions (see Table II).

Fig. 4 shows the LSTs of different surfaces at 7:00, 10:00, 12:00, and 19:00 in July, which can clearly and intuitively reflect the temperature distributions and variation characteristics of different surfaces at different times.

Meteorological data include air temperature, humidity, wind speed, wind direction, and solar radiation. Ten wireless temperature and humidity sensors are placed in the observation area and placed in a louver box to obtain real-time near-surface and air temperature and humidity data at intervals of 5 min (the position of the sensor has been marked in red in Fig. 1). The wind speed and wind direction data in the study area were obtained using a hand-held anemometer, and the solar radiation was observed using a CNR4 solar radiation meter. The HOBO MX2201 thermometer and a hand-held noncontact infrared thermometer Raytek MT6 were used to measure the water and artificial LSTs; the temperature measurement accuracy was within 1 °C to verify the accuracy of the thermal infrared data of the UAV.

III. METHODS

A. UAV Thermal Infrared Data Acquisition and Processing

1) Camera Calibration and Data Acquisition: The factors affecting the accuracy of the thermal imager include the physical properties of the object being measured, the weather conditions, and the flying height of the drone. Therefore, the thermal infrared imager should be calibrated before data acquisition. The main problem affecting the accuracy of the thermal imager is the specific emissivity of the surface. Wu [45] mentioned the use of hand-held thermal infrared cameras to study the thermal characteristics of common surface types in typical residential areas. Different surfaces have different emissivity, but because of their various properties, measurement is difficult, and the ground material involved in the study has higher specific emissivity. Therefore, the bright temperature values are used as the actual temperatures, and no corrections are made. According to the data, the average specific emissivity of the surface involved in this study is between 0.93 and 0.98. To obtain accurate ground specific emissivity, Voogt and Oke measured the radiance of common roads such as asphalt roads, concrete, and vegetation [47]. The measurement method was proposed by Chen and Zhang [19]. The measurement results showed that the values of the specific emissivity measured at different observation points are different, but that the difference is small, and the total emissivity is between 0.92 and 0.98. In addition, most of the existing infrared temperature measurement products set the specific emissivity to 0.95 by default. Therefore, when using the thermal infrared imager to obtain the LST data in the study, the specific emissivity is set to 0.95 in the imager-specific system.

We first used the tilt to fix the imager to the UAV. Before the drone was taken off, the ground station was used to design the route and flight parameters. Due to the small scope of the study area, only one route was designed in the experiment, and the flight height was set to 180 m. To ensure the integrity of the image mosaic, the overlap was set to 80%.

After setting the various parameters of the UAV, it is necessary to set the parameters of the thermal infrared camera. The imager was set up by connecting the camera via Bluetooth, and the color palette can be changed, and image optimization features can be set. The thermal infrared camera used in the experiment is a special camera for UAVs. The measurement error caused by the flying height has been considered in the design of the camera system. Therefore, before taking a picture using the camera, the system parameters were first set, including real-time weather conditions (sunny, cloudy), air temperature, relative humidity, and flying height to provide image correction. After data acquisition, the camera analysis software combined with meteorological data can be used to analyze and calibrate the thermal infrared image to improve the accuracy of the temperature observations.

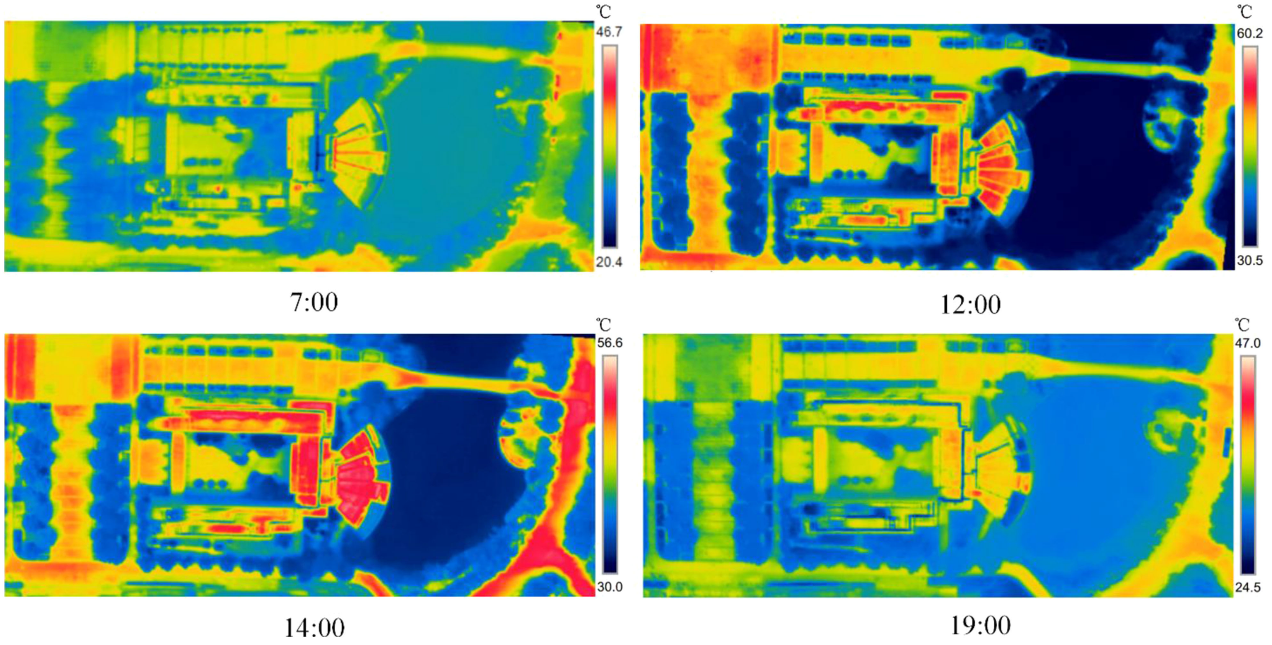

7:00 12:00

14:00 19:00

Fig. 4. LSTs of different surfaces at different times in July.

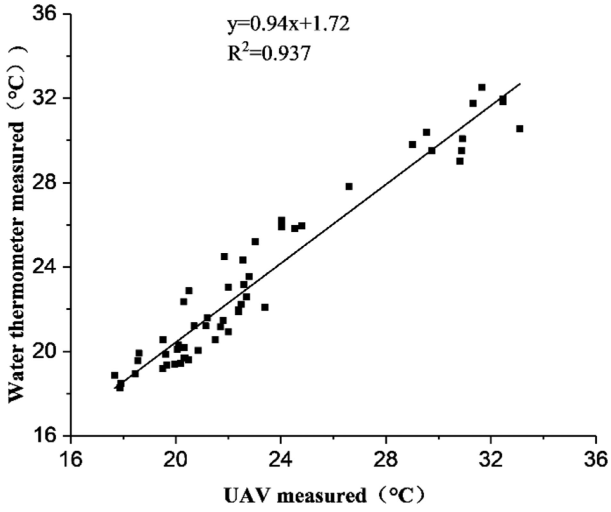

Fig. 5. Comparison of water temperatures measured by infrared imager and water thermometer.

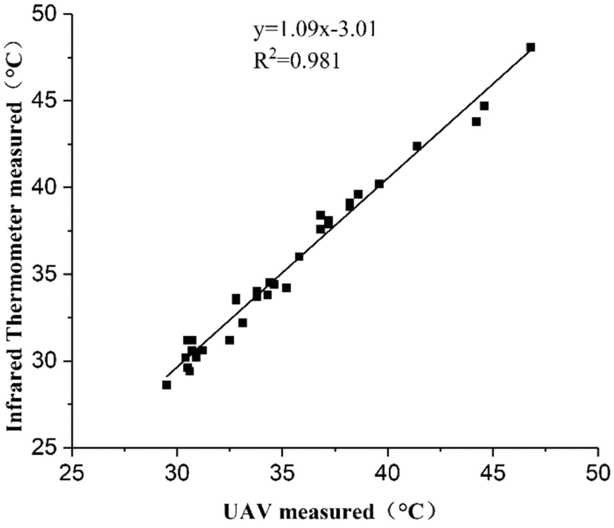

Fig. 6. Comparison of artificial surface temperatures measured by infrared imager and infrared thermometer.

Each time data are acquired, this task should be completed within 5 min to reduce errors caused by rapid temperature changes.

2) Precision Verification: To verify the accuracy of the data obtained by the UAV thermal imaging system, regression analysis was performed on the water temperature measured by the HOBO MX2201 thermometer and the temperature of the water measured by the thermal imager (see Fig. 5). The linear regression coefficient between the two methods was 0.937. The regression fitting result was good, and the error was mainly within 1 °C, which met the accuracy requirements of the experiment. In addition, Raytek MT6 infrared thermometer is used to verify the accuracy of artificial surface temperature obtained by thermal infrared camera (see Fig. 6). The linear regression coefficient between the two methods was 0.981. The regression fitting result was good, and the error was mainly within 1 °C. This error was within the allowable range.

Additionally, thermal infrared images of the same surface at flight heights of both 10 and 180 m were acquired and analyzed in the same time period. The results showed that the difference in LSTs of the same surface at different flight heights is very small, and the maximum difference does not exceed 1 °C. This error was within the allowable range, and the accuracy of the image correction by the thermal infrared camera system met the experimental requirements.

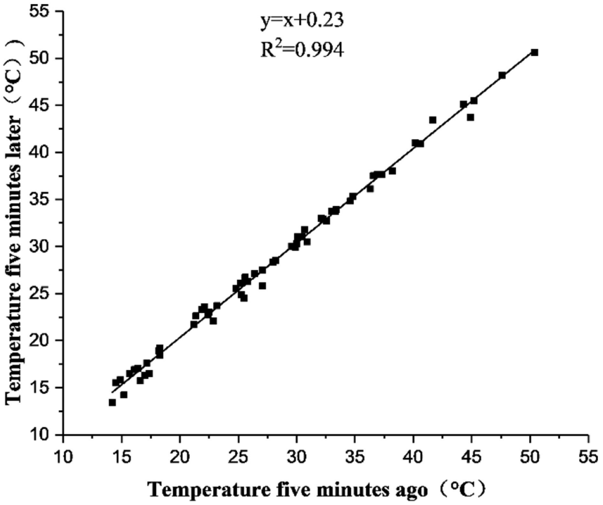

Fig. 7. Comparison of LSTs before and after 5 min.

Since the temperatures change rapidly under high temperature conditions, the data were acquired in 5 min windows. This can be achieved when designing the route, and each image had a specific time for image capture. To verify that the temperature difference for the same surface was not evident during the 5 min interval, regression analysis was carried out to extract the temperature values of different surfaces under different weather conditions and at different times at 5 min intervals. The linear regression coefficient between the temperature values before and after the time interval was 0.994 (see Fig. 7), and the degree of fit was high, with an average error of 0.23 °C. This indicated that the LST changes little during the time interval, so it was feasible to use images obtained within a 5 min span for mosaicking when extracting the LST of different surfaces.

3) Data Processing: The images acquired by UAV thermal infrared camera were processed by dedicated software FLIR Tools. The clear images were then selected for mosaicking from the multiple acquired images to obtain a panoramic view of the study area. First, the surface specific emissivity was input at the time of data acquisition, and the atmospheric corrections and accuracy verifications were performed. Due to this data processing, the images acquired by the thermal infrared camera were able to reflect the real LSTs. The temperature of each pixel in the image can then be directly obtained after being calibrated in the software. Sampling uniformly for different surfaces was important for avoiding errors resulting from a single sample. Ten sample areas are selected for each surface type, and then the average temperature values of ten sample areas are averaged. Finally, we can get the temperature values of different surface at each time. Finally, statistical analysis of the data was carried out in conjunction with the meteorological data.

B. Sensible Heat Flux Calculation

Sensible heat is the exchange of heat in the form of turbulence between the atmosphere and the surface caused by temperature changes in an object or in a thermal system [48], [49]. Two main factors affect sensible heat release: one is the difference between LST and air temperature; the other is the flow velocity of air. Higher wind speeds cause stronger surface air turbulence and higher sensible heat release. The sensible heat flux calculation formula is as follows [50]:

$$H = h_c(T_s - T_a) \tag{1}$$

where H is the sensible heat flux, T_s is the LST, T_a is the air temperature, and h_c is the heat convection. The following empirical formula can provide reasonable accuracy for h_c [51]:

$$h_c = \begin{array}{ll} 5.6 \times 4.0v & v < 5 \\ 7.2 \times v^{0.78} & v \geq 5 \end{array} \tag{2}$$

where v is the wind speed measured at 9.0 m height. In the experiment, the height used for observing the wind speed was 1.5 m. To obtain the wind speed at 9 m, the wind profile index law can be used to convert the wind speed [52]

$$\bar{u} = \bar{u}_1 \left[\frac{z}{z_1}\right]^m \tag{3}$$

where $\bar{u}_1$ is the average wind speed at the known height of z_1, $\bar{u}$ is the average wind speed at the desired height of z, and m is the stability parameter, which refers to the stability of the atmosphere. By judging the atmospheric stability of the study area, the value of m is 0.25.

IV. RESULTS

A. LST Variation Characteristics and Sensible Heat Release of Different Surfaces

1) Diurnal Variation in LSTs Under Different Weather Conditions: Solar radiation intensities under different weather conditions presented large differences, which have a large impact on LST. Using the data from two consecutive days in April, the variation characteristics of the LST of the surfaces under different weather conditions were compared. Under sunny conditions, the diurnal variation trends in LST of six surfaces were very similar. The temperatures were lowest at 7:00 in the morning and gradually increased after 7:00. Within the time range of 12:00–14:00, the LSTs reached a peak, and the LST of each surface gradually decreased after 14:00 due to decreases in the solar radiation intensity [see Fig. 8(a)]. However, the rates of LST variation for different surfaces were noticeably different. The LST variations in the artificial surfaces were clearly larger than those of the natural surfaces, especially water bodies and tree canopy. The highest LST of the artificial surfaces was higher than that of the natural surfaces by approximately 20 °C, and the maximum daily difference was 29.03 °C (see Table III). For the artificial surfaces, the LST variation showed a daily change due to the different materials comprising the surface. The LST of the asphalt pavement remained the highest among all surfaces starting at 8:00 in the morning, followed by the brick pavement, while the marble pavement was relatively low. The maximum LSTs of asphalt pavement, brick pavement, and marble pavement for one day were 45.68, 42.71, and 39.63 °C, respectively, indicating that the asphalt pavement had the largest impact on the urban thermal environment under the same illumination and weather

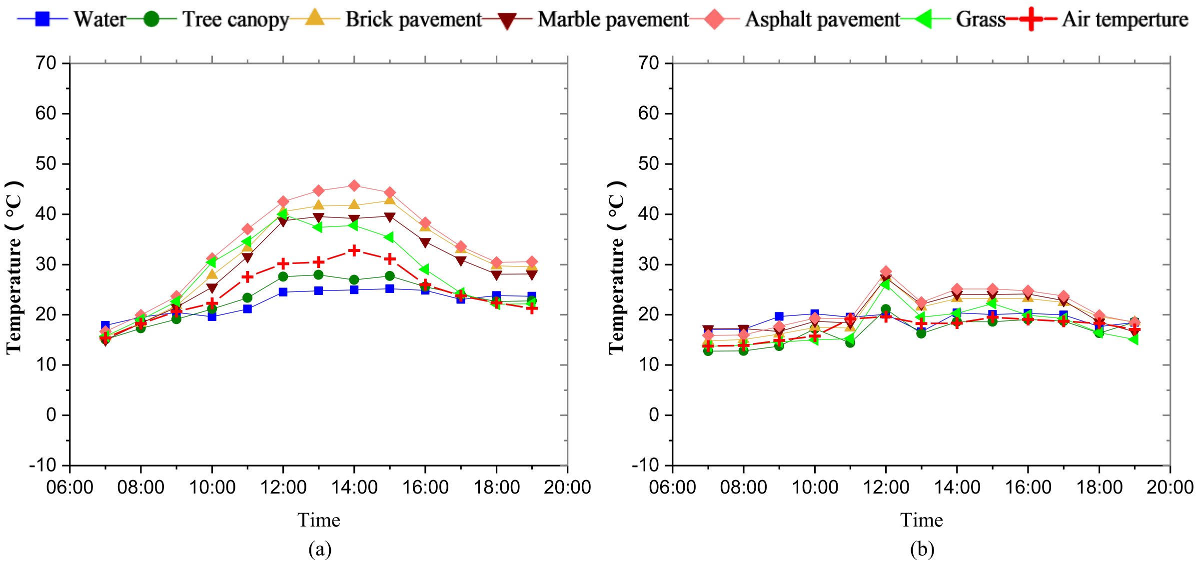

(a) (b)

Fig. 8. Diurnal variation in LST under different (a) sunny days and (b) cloudy conditions.

TABLE III
LST AND AIR TEMPERATURE FOR DIFFERENT SURFACES (°C)

Weather condition	Item	Water	Tree canopy	Grass	Brick pavement	Marble pavement	Asphalt pavement	Air temperature
Cloudy （4.24）	Average	18.93	16.81	18.07	20.18	20.78	21.38	17.32
	Maximum	20.36	21.1	26	27.5	27.3	28.6	19.62
	Minimum	16.6	12.79	13.72	14.8	16.6	15.88	13.78
	Diurnal range	3.76	8.31	12.28	12.7	10.7	12.72	5.84
Sunny （4.25)	Average	22.43	22.95	28.42	31.43	29.68	33.40	24.69
	Maximum	25.17	27.93	40	42.71	39.63	45.68	32.78
	Minimum	17.89	15.08	15.7	15.56	14.97	16.65	15.41
	Diurnal range	7.28	12.85	24.3	27.15	24.66	29.03	17.37

conditions. For the natural surfaces, the daily LST variation in the water body is the lowest, and the daily difference was 7.28 °C. Because the water body has a larger specific heat capacity and a stronger heat absorption capacity, the solar radiation does not cause a drastic change in the LST of water bodies. The LST variation in tree canopy was relatively low. The maximum LST for tree canopy was 27.9 °C, and the daily difference was 12 °C. The LST of grass reached 40 °C at 11:00, which was close to the artificial LSTs. The LST of grass was much higher than the water body and tree canopy temperatures.

The relationship between LST and air temperature is a key factor affecting the urban thermal environment. At the same time, it can clearly and intuitively reflect the surface heat absorption and heat release. Fig. 8(a) shows that the change trend of the LST for the six surfaces was consistent with the air temperature. Before 9:00, the LST of the water was slightly higher than the air temperature. Then, the LST gradually rose, and after 10:00, it was significantly higher than the LST of water, and the highest LST difference reached up to 5.6 °C, indicating that the water body had a strong cooling effect. The LST of the tree canopy remained below the air temperature during the day, and they absorb heat from the atmosphere, lowering the air temperature. This is also an important reason for utilizing the method of planting green plants in response to the heat island effect. Compared with water bodies and tree canopy, the cooling effect of grass as a green plant was not evident. The LST of grass during the day was almost higher than the air temperature and it has the effect of increasing air temperature to a certain extent. For the artificial surfaces, the LSTs of the three surfaces were significantly higher than the air temperature. Among these, the highest asphalt can be higher than the temperature of 11 °C, indicating that the effect of temperature increase was most notable. The maximum difference between the LSTs and the air temperature can reach 10 °C for marble and brick pavement, which also had a strong warming effect. The above conclusions further demonstrate that the formation of UHIs (Urban Heat Islands) is closely related to the urban impervious surface. Through the analysis of the data obtained in July, the difference between the LST and the air temperature for artificial surfaces was no more than 20 °C at noon, and a maximum temperature difference of 10 °C took place during a sunny day in April.

Under cloudy conditions, daily variations in the LSTs of the six surfaces were not obvious. The daily differences were between 3 and 12 °C. The LSTs of the artificial surfaces were

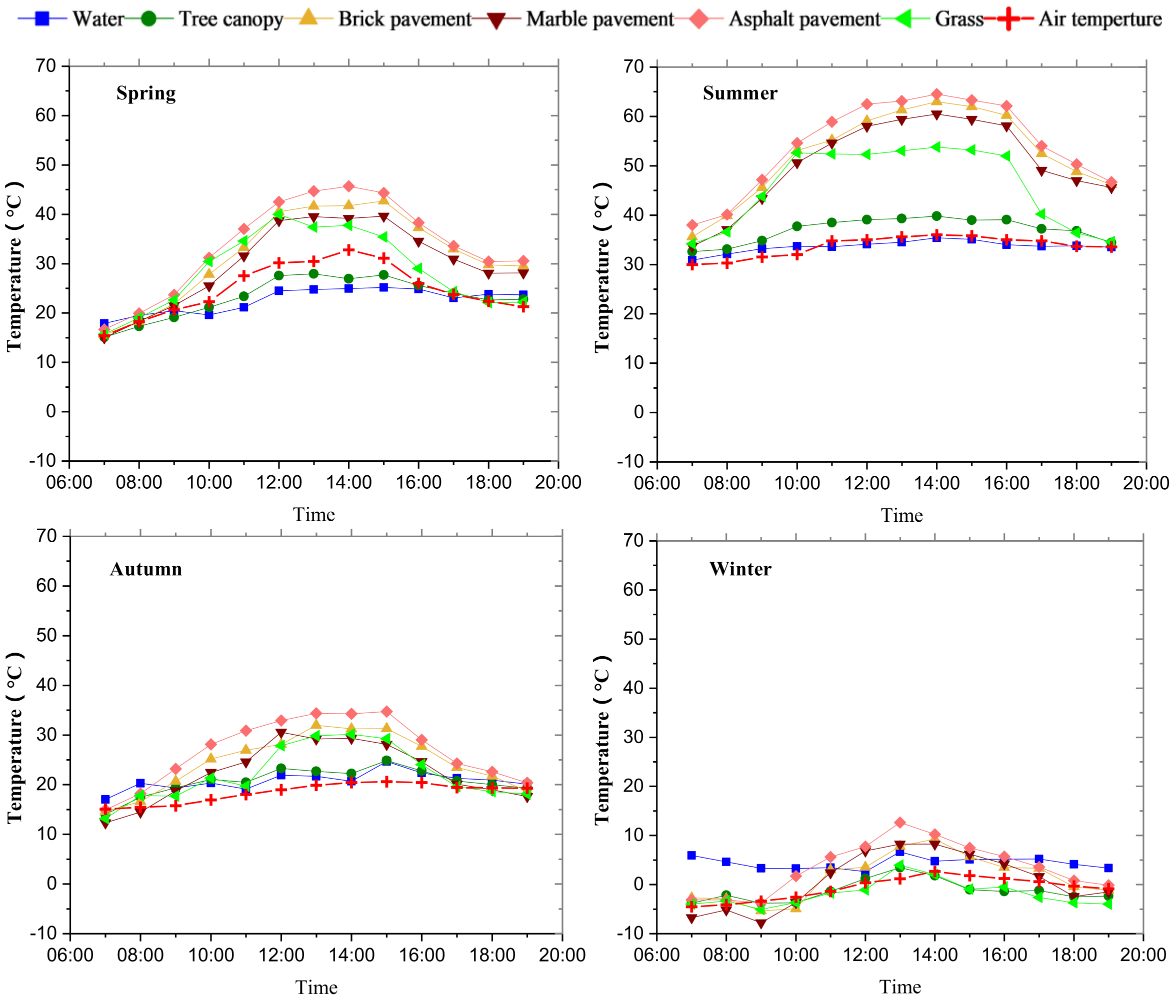

Fig. 9. Seasonal variations in LSTs of the surfaces.

more sensitive to solar radiation than the natural surfaces [see Fig. 8(b)]. Before enhancement by solar radiation, the water body had the highest LST, which was 2–3 °C higher than the other surfaces. After this, the artificial LSTs increased rapidly and were higher than the natural LSTs by an average of approximately 5 °C. For natural LSTs, the increase was small and the variation was not notable.

2) Characteristics of Different Seasons Under Sunny Conditions: The LST data of the surfaces under different sunny conditions in different seasons were selected to study the seasonal variability of the LSTs of the urban surface. Fig. 9 shows that the daily change trend of the LST in a day was basically the same in different seasons, showing a trend of increasing first and then gradually decreasing after reaching a peak value. There is also a significant difference in surface temperature between different seasons.

Summer LSTs were the highest, and the LSTs of the surface were also significantly higher than in other seasons. The artificial LSTs raised rapidly, the highest LST reached up to 64.5 °C, and the daily difference was 26.8 °C. From 10:00 A.M. to 5:00 P.M., the three artificial LSTs were above 50 °C; the asphalt pavement was the hottest, followed by the brick pavement and the marble pavement, which was hotter than the air temperature by 10 °C. The LST of grassland increased before 9:00 A.M. and was consistent with that in the artificial surfaces. Relative to water bodies and tree canopy, the LST of grassland raised rapidly and was still 10 °C higher than LSTs of the water body and tree canopy between 10:00 and 17:00 but was lower than LST of the artificial surfaces by 5–10 °C. This showed that although the cooling effect of the lawn was not as large as that of tree canopy and water bodies under high LSTs, the warming effect was far lower than that for artificial surfaces. The LSTs of water bodies and tree canopy were significantly lower than those of artificial surfaces and lawns, and were stable within one day, and the maximum LST did not exceed 40 °C.

The differences for LSTs of the six surfaces in winter were not obvious, and the daily average LSTs were between –1.9 and 4.4 °C (see Fig. 10). The average LSTs, from high to low, were for water, asphalt pavement, brick pavement, marble pavement, tree canopy, grass. The artificial surface LSTs were as high as 12.64 °C and were as low as –7.8 °C and were higher than the LST of water body between 11:00 and 16:00, and at other

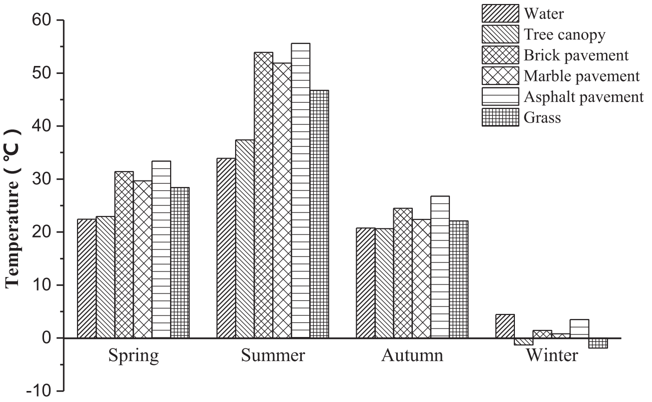

Fig. 10. Seasonal variation in average LSTs of the surfaces.

times were lower than the LST of water body. For the natural surfaces, the LSTs of the tree canopy were the lowest and were also lower than the air temperature, which, to some extent, has a cooling effect. The change in LSTs of the grassland in winter was clearly different from that in summer. Affected by factors such as growth conditions and soil moisture, the average grassland temperature was the lowest among the six surfaces. However, the daily changes were more stable, which was consistent with the tree canopy. The average LST of the water body was the highest in winter, and the LST is higher than the air temperature during the daytime. In contrast to summer, there was a significant increase in temperature.

The changes of LST in the surfaces in spring and autumn were similar. The daily average LSTs were between 20.6 and 33.1 °C. The average LSTs of artificial surfaces were 4–9 °C higher than for natural surfaces and were still the main sources of heat release. The above studies showed that the influence of urban LST changes on the thermal environment is more obvious and representative in sunny days.

3) Sensible Heat Release of Different Surface Types: There were differences in the sensible heat flux between different surfaces for different weather conditions or in different seasons. From (1), it is known that the sensible heat flux value is related to the temperature difference between the surface and the atmosphere and the wind speed. When the LST is higher than the air temperature, the sensible heat flux value is positive, and the sensible heat flux is transmitted from the ground to the colder air above and promotes its heat increase. When the LST is lower than the air temperature, the sensible heat flux is negative, and heat is transferred from the air to the ground and causes the air to cool.

Fig. 11 shows the sensible heat release and wind speed at different times in different weather conditions in spring. The value of sensible heat release fluctuated with the wind speed, indicating that the wind speed had a large influence on the sensible heat release. However, another important factor affecting the amount of sensible heat release was the difference between the LST and the atmosphere temperature. Therefore, when the wind speed is maximum, the level of sensible heat release is not necessarily the highest. As shown in Fig. 10(b), the wind speed was the highest at 10:00 for one day but the peak of the heat release was reached at 12:00. Because the LST was significantly higher than the air temperature at 12:00, the effect of the temperature difference on the amount of heat release exceeded the effects of wind speed. These two factors should be considered together to determine the amount of sensible heat release.

Because of the strong solar radiation on sunny days, the LSTs increased rapidly, and the difference between the LST and the atmosphere temperatures was more obvious than for cloudy conditions. The heat released by the four different surfaces at the same time was also different, and the artificial surface heat release is significantly higher than that of the grass. On sunny days, the sensible heat release of the grass at a certain time did not exceed 100 W/m^2, while the sensible heat of artificial surface released more than 100 W/m^2 between 11:00 and 17:00, with levels as high as 280 W/m^2. The surface of asphalt pavement released the most sensible heat during the day, which was 5–60 W/m^2 higher than the brick and marble pavements under the same conditions. The LST of the grass was higher than the air temperature, and there was a certain amount of sensible heat release. However, grassland, as vegetation, exhibited the transpiration by the leaves and the evaporation of the soil make the sensible heat release of the grassland lower than that of the artificial surface.

Under the same weather conditions, there were also large differences in the amount of sensible heat released in different seasons. We used the two typical seasons (summer and winter) as a comparative experiment. As shown in Fig. 12, in the summer, since the observation day was in a windless state, the amount of sensible heat release mainly depended on the difference between the LST and the air temperature. In summer, the LST of water body was lower than the air temperature, so its sensible heat release was negative, indicating that the summer water body mainly absorbs heat during the day. The LST of the tree canopy was slightly higher than the air temperature, and the maximum amount of sensible heat was not more than 40 W/m^2. The sensible heat release of artificial surfaces and grass was significantly higher than that of water bodies and tree canopy, with artificial grounds exceeding 100 W/m^2 between 10:00 and 16:00. As natural surfaces, grasslands have a higher heat release than water bodies and tree canopy in summer, while in winter is closer to tree canopy. Therefore, the influence of grassland on thermal environment varies with season.

In winter, the LSTs of the grass and tree canopy were lower than the air temperature, and the amount of heat release was negative, leading to heat absorption. The LST of the water was higher than the air temperature in winter, and the sensible heat release reached 100 W/m^2 in windy conditions. Contrary to what occurs in summer, the water body mainly released heat in winter. The artificial surfaces were similar in winter to the other seasons. Affected by the differences in temperature and wind speed, they still exhibited high sensible heat release at noon. However, because the difference between LST and air temperature was significantly lower than that in summer, the sensible heat release was generally lower in winter than in summer.

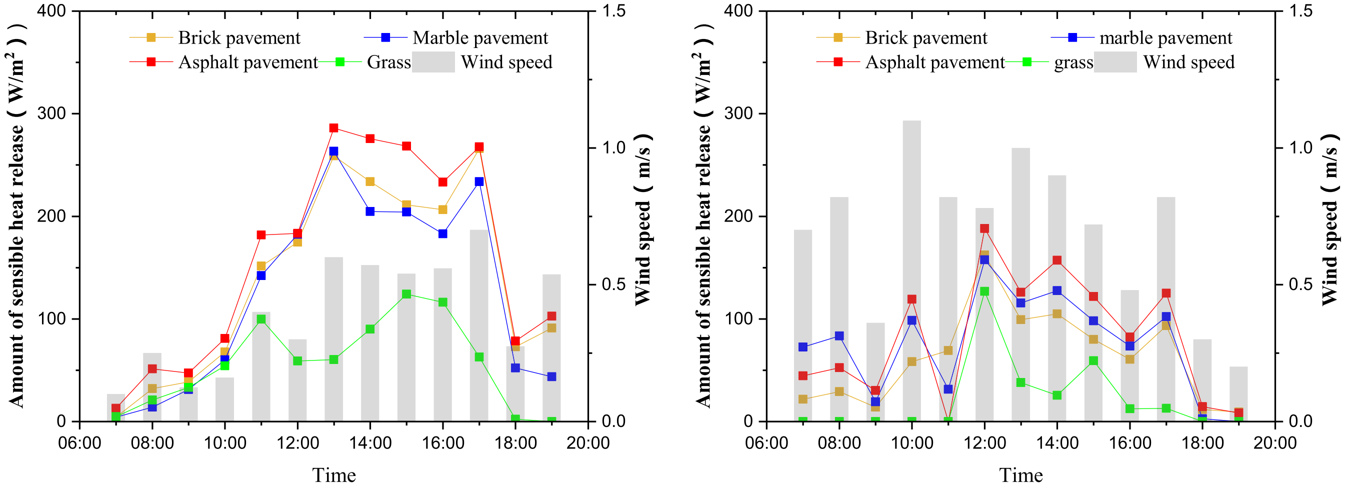

(a) (b)

Fig. 11. Sensible heat fluxes of the surfaces at different times on (a) sunny days and (b) cloudy days.

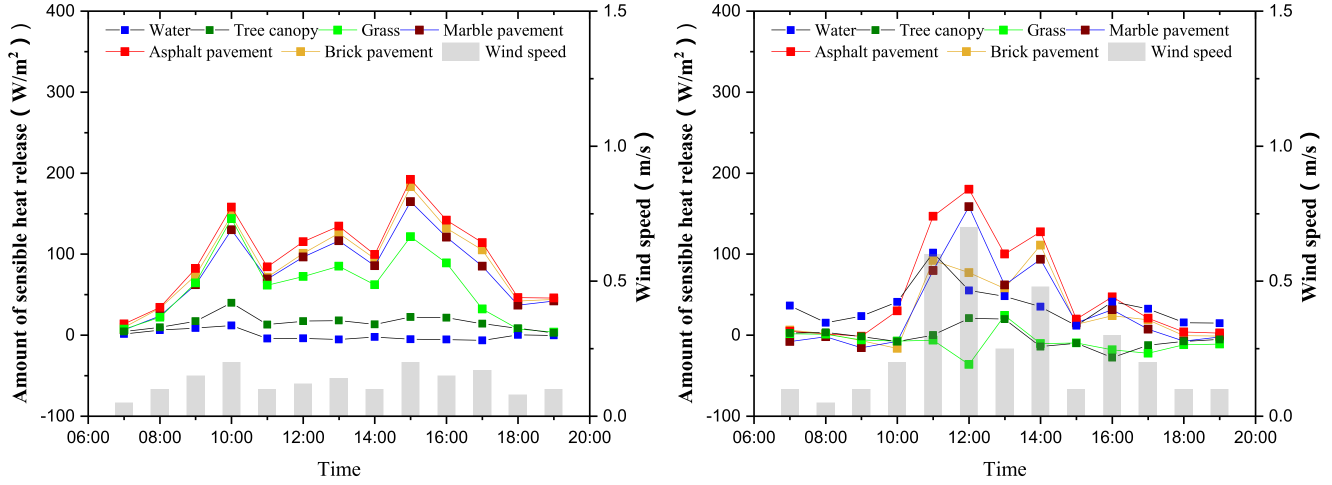

(a) (b)

Fig. 12. Sensible heat release in different seasons. (a) Summer. (b) Winter.

B. Factors Affecting LST in Different Surfaces

1) Correlation Analysis Between LSTs and Meteorological Factors: Using sunny weather as an example, the correlation between the LSTs and various meteorological factors was analyzed. Table IV shows the correlation between meteorological factors and LSTs for different surfaces.

Solar radiation and air temperature were positively correlated with LST, and the air temperature correlation coefficient was higher than that of solar radiation. The correlation coefficient between air temperature and the LST of each surface was mostly above 0.87, which indicates a strong correlation. Water bodies and grass were significantly correlated with solar radiation at a 0.05 level, which was lower than the relationship between LSTs and solar radiation for the artificial surface. This means that solar radiation has a larger impact on artificial surfaces. This is also the reason why artificial surfaces have a larger impact on the UHI effect in summer. There was a significant negative correlation between the LSTs of the six surfaces and the air humidity. The higher water vapor content weakened the effects of solar radiation during the day and had a certain inhibitory effect on surface warming. There was no significant correlation between wind speed and LST.

2) Effect of Shadows on LSTs: For the thermal balance of the surface, the heat from the solar radiation is a large proportion of the effect, especially in the summer with strong UHI effects. Correctly dealing with the influence of the day shadow effect on the LSTs is of major significance to the study of the urban thermal environment. In the microclimate of residential areas, due to dense construction, buildings and tree canopy form a large proportion of shadows on the surface for the case of direct sunlight. The surfaces are an important part of the urban microenvironment, and shadows have a significant influence on

TABLE IV
CORRELATION COEFFICIENTS OF LST AND METEOROLOGICAL FACTORS FOR SURFACES

Meteorological factors	Correlation coefficient					
	Water	Tree canopy	Grass	Brick pavement	Marble pavement	Asphalt pavement
Solar radiation	0.576*	0.640*	0.759**	0.637**	0.704**	0.711**
Air temperature	0.933**	0.936**	0.625*	0.912**	0.872**	0.874**
Air humidity	-0.890**	-0.871**	-0.521**	-0.845**	-0.824**	-0.807**
Wind speed	0.793**	0.703	0.174	0.547	0.502	0.481

**A significant correlation at the level of .01 (bilateral). *A significant correlation at the level of 0.05 (bilateral).

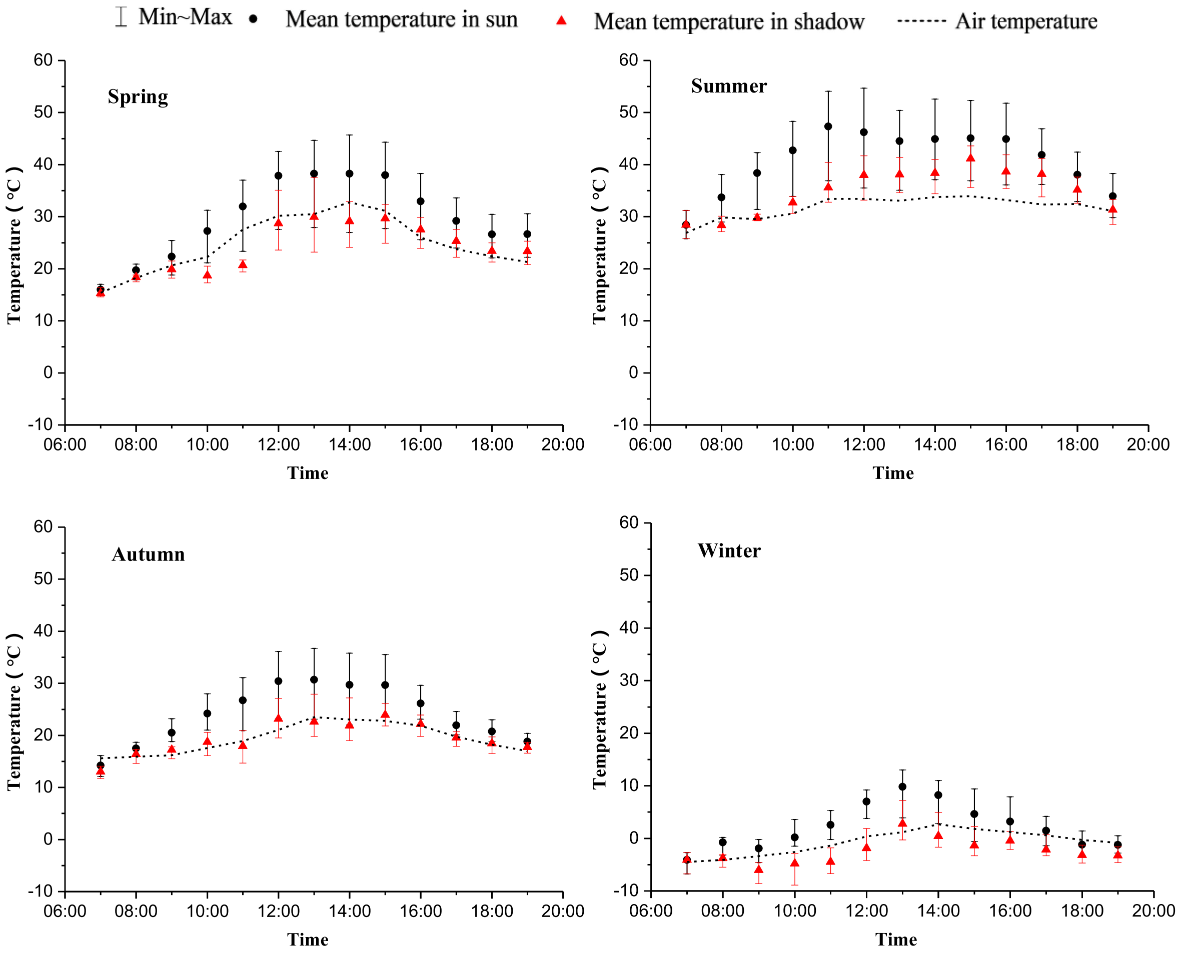

Fig. 13. Effect of shadow on LST in different seasons.

the temperature of the surfaces over a large area. Therefore, dealing with the shadow effect has a high impact on the study of the microthermal environment. Using the image data acquired by the UAV, the LSTs of the different surfaces in the shaded and non-shaded areas can be extracted.

Since the water bodies are less affected by the sun, only the effects of the sun shadow on tree canopy, grass, and artificial surfaces are discussed here. The LSTs of the surfaces were very different between the shaded and non-shaded areas. As shown in Fig. 13, min and max refer to the minimum and maximum of the five surface temperatures. Under different seasonal conditions, the change of LST under shadows was consistent with the LST under the sun, showing a trend of increasing first and then decreasing. However, the LSTs in the shadows were lower than the LSTs under the sun, and the difference is largest between 12:00 and 15:00, and the largest difference was 15 °C. Among the six surfaces, shadows have less effect on tree canopy and have the largest impact on the asphalt in the artificial surfaces.

In spring and autumn, the average LSTs of different surfaces in non-shaded areas were 2–8 °C higher than that of shadowed areas. The average LSTs in the shaded area were close to the air temperature, and the average LSTs in the non-shaded area were higher than the air temperature by 0–11 °C. This showed that in the spring and autumn, the warming and cooling effects of different surfaces in the shaded area were mutually neutralized, and no effective temperature increase, or cooling occurs. The warming effect mainly came from the non-shaded areas. In summer, the average LST in the unshaded areas was 1–9.7 °C higher than that in the shaded areas. The minimum LST in the shaded areas was closest to the air temperature, while the LSTs in the non-shaded areas were higher than the air temperature. This showed that both the shaded areas and the non-shaded areas show warming in the summer, and the effect of warming in the non-shaded areas is more obvious. In winter, the average LST in the non-shaded areas was higher than that in the shaded areas by 2.3–6.7 °C, which was lower than summer and autumn, indicating that the influence of the shadows on the LSTs was smaller than for other seasons. This was because the solar radiation is weak in winter, which causes the surface to be influenced less by solar radiation and cannot exhibit an effective temperature rise under the influence of the sun. In addition, the lowest LST in the non-shaded area and the highest LST in the shaded area were close to the air temperature, indicating that there was a certain warming effect in the non-shaded area in winter, and the shaded area has a cooling effect. In densely populated areas, the shaded areas are larger than the non-shaded areas, resulting in a net cooling effect.

V. DISCUSSIONS

In the past, most scholars have used remote sensing data to study urban thermal environments. At present, most of the thermal infrared data come from satellite observations. The spatial resolution of the data is mostly over 30 m, which makes it impossible to accurately acquire the surface temperature data of different surfaces in a small urban area. In addition, due to the limited spatial and temporal resolution of remote sensing thermal infrared data, it is impossible to carry out refined urban thermal environment research.

As a new industry, UAV has the advantages of flexible operation, easy learning, and low cost. First, UAV equipped with a thermal infrared camera has the convenience of collecting data and solves the problem of large data acquisition by using a hand held thermal infrared camera. Second, in urban areas, the suitability of thermal infrared imagery obtained from UAV is seldom explored. Therefore, the use of UAV to analyze the temperature variations of different urban surfaces under various conditions at small scale is the new idea to get the more detailed information for the study of micro-scale urban thermal environments.

On the other hand, there are also some shortcomings in the acquisition of surface temperature data by the thermal infrared camera of UAV, such as the short duration of the UAV, the photo distortion caused by the flight attitude instability, which will affect the accuracy of temperature measurement. In addition, the weather has a greater impact on the UAV. Therefore, the experiment should be carried out under specific weather conditions. In addition, the problem of the surface emissivity still exists in our research. Different surfaces have different emissivity, and there are differences in LSTs at different periods. Therefore, obtaining accurate specific emissivity is crucial for improving the accuracy of thermal infrared data.

In the future, the combination of multiple radiative properties of surfaces and urban morphology aspects will be considered. We will select different research areas and use numerical simulation method to study the thermal environment under different urban morphology. In addition, the building information modeling can be combined with UAV technology to precisely simulate the urban microenvironment and explore urban thermal environment problems under different building conditions to provide a reference for urban construction and planning.

VI. CONCLUSION

In this article, the thermal infrared images of UAV were used as the data source to analyze the detailed characteristics of daily and seasonal variations in LSTs for different surfaces in a typical urbanized area. Then, combined with the measured meteorological data, the meteorological factors affecting the LST were identified and the influence mechanism on the thermal environment is analyzed.

ACKNOWLEDGMENT

The authors would like to thank all the organizations for sharing data.

REFERENCES

[1] Y. Liu and W. Quan, “Research on high temperature indices of Beijing city and its spatiotemporal pattern based on satellite data,” *Climatic Environ. Res.*, vol. 19, no. 3, pp. 332–342, 2014.

[2] J. A. Voogt and T. R. Oke, “Thermal remote sensing of urban climates,” *Remote Sens. Environ.*, vol. 86, no. 3, pp. 370–384, 2003.

[3] L. Y. Wu, “Expectations of 21st century architecture-source material of the Beijing Chapter,” *Architectural J.*, vol. 4, pp. 1–18, 1998.

[4] J. M. A. Duncan, B. Boruff, A. Saunders, Q. Sun, J. Hurley, and M. Amati, “Turning down the heat: An enhanced understanding of the relationship between urban vegetation and surface temperature at the city scale,” *Sci. Total Environ.*, vol. 656, pp. 118–128, 2019.

[5] F. Yuan and M. E. Bauer, “Comparison of impervious surface area and normalized difference vegetation index as indicators of surface urban heat island effects in Landsat imagery,” *Remote Sens. Environ.*, vol. 106, no. 3, pp. 375–386, 2007.

[6] Q. Weng, P. Fu, and F. Gao, “Generating daily land surface temperature at Landsat resolution by fusing Landsat and MODIS data,” *Remote Sens. Environ.*, vol. 145, pp. 55–67, 2014.

[7] J. Li, C. Song, L. Cao, F. Zhu, X. Meng, and J. Wu, “Impacts of landscape structure on surface urban heat islands: A case study of Shanghai, China,” *Remote Sens. Environ.*, vol. 115, no. 12, pp. 3249–3263, 2011.

[8] X. Chen, H. Zhao, P. Li, and Z. Yin, "Remote sensing image-based analysis of the relationship between urban heat island and land use/cover changes," *Remote Sens. Environ.*, vol. 104, no. 2, pp. 133–146, 2006.

[9] J. Hansen, R. Ruedy, and M. Sato, "Global surface temperature change," *Rev. Geophys.*, vol. 48, no. 4, 2010, Art. no. RG4004.

[10] P. D. A. Kraaijenbrink, M. F. P. Bierkens, A. F. Lutz, and W. W. Immerzeel, "Impact of a global temperature rise of 1.5 degrees Celsius on Asia's glaciers," *Nature*, vol. 549, no. 7671, pp. 257–260, 2017.

[11] C. Aubry-Wake *et al.*, "Measuring glacier surface temperatures with ground-based thermal infrared imaging," *Geophys. Res. Lett.*, vol. 42, no. 20, pp. 8489–8497, 2015,

[12] K. Li, Y. Chen, M. Wang, and A. Gong, "Spatial-temporal variations of surface urban heat island intensity induced by different definitions of rural extents in China," *Sci. Total Environ.*, vol. 669, pp. 229–247, 2019.

[13] M. C. Anderson, R. G. Allen, A. Morse, and W. P. Kustas, "Use of Landsat thermal imagery in monitoring evapotranspiration and managing water resources," *Remote Sens. Environ.*, vol. 122, pp. 50–65, 2012.

[14] I. Colomina and P. Molina, "Unmanned aerial systems for photogrammetry and remote sensing: A review," *ISPRS J. Photogramm.*, vol. 92, pp. 79–97, 2014.

[15] D. Li and M. Li, "Research advance and application prospect of unmanned aerial vehicle remote sensing system," *Geomatics Inf. Sci. Wuhan Univ.*, vol. 39, no. 5, pp. 505–513, 2014.

[16] C. Zhang and J. M. Kovacs, "The application of small unmanned aerial systems for precision agriculture: A review," *Precision Agric.*, vol. 13, no. 6, pp. 693–712, 2012.

[17] J. A. J. Berni, P. J. Zarco-Tejada, G. Sepulcre-Canto, E. Fereres, and F. Villalobos, "Mapping canopy conductance and CWSI in olive orchards using high resolution thermal remote sensing imagery," *Remote Sens. Environ.*, vol. 113, no. 11, pp. 2380–2388, 2009.

[18] A. Urbahs and I. Jonaite "Features of the use of unmanned aerial vehicles for agriculture applications," *Aviation*, vol. 17, no. 4, pp. 170–175, 2013.

[19] J. M. Chen and R. H. Zhang, "Studies on the measurements of crop emissivity and sky temperature," *Agricultural Forest Meteorol.*, vol. 49, no. 1, pp. 23–34, 1989.

[20] K. Iizuka, T. Yonehara, M. Itoh, and Y. Kosugi, "Estimating tree height and diameter at breast height (DBH) from digital surface models and orthophotos obtained with an unmanned aerial system for a Japanese cypress (*Chamaecyparis obtusa*) forest," *Remote Sens.*, vol. 10, no. 131, pp. 13–27, 2018.

[21] S. Z. Cui and J. G. Zhou, "Application of UAV aerial system on surveying and mapping of topographic map at scale 1:1000," *Surveying Mapping Geol. Mineral Resour.*, vol. 4, pp. 29–31, 2014.

[22] N. Homainejad and C. Rizos, "Application of multiple categories of unmanned aircraft systems (UAS) in different airspaces for bushfire monitoring and response," *Int. Archives Photogrammetry, Remote Sens. Spatial Inf. Sci.*, vol. 40, pp. 55–60, 2015.

[23] U. Niethammer, M. R. James, S. Rothmund, J. Travelletti, and M. Joswig, "UAV-based remote sensing of the super-Sauze landslide: Evaluation and results," *Eng. Geol.*, vol. 128, pp. 2–11, 2012.

[24] W. W. Immerzeel *et al.*, "High-resolution monitoring of Himalayan glacier dynamics using unmanned aerial vehicles," *Remote Sens. Environ.*, vol. 150, pp. 93–103, 2014.

[25] P. D. A. Kraaijenbrink *et al.*, "Mapping surface temperatures on a debris-covered glacier with an unmanned aerial vehicle," *Frontiers Earth Sci.*, vol. 6, pp. 64–83, 2018.

[26] K. Anderson and K. J. Gaston, "Lightweight unmanned aerial vehicles will revolutionize spatial ecology," *Frontiers Ecol. Environ.*, vol. 11, no. 3, pp. 138–146, 2013.

[27] L. P. Chrétien, J. Théau, and P. Ménard, "Wildlife multispecies remote sensing using visible and thermal infrared imagery acquired from AN unmanned aerial vehicle (UAV)," *Int. Archives Photogrammetry, Remote Sens. Spatial Inf. Sci.*, vol. 40, pp. 241–248, 2015.

[28] P. J. Zarco-TejadaV. Gonzalez-Dugo and J. A. J. Berni, "Fluorescence, temperature and narrow-band indices acquired from a UAV platform for water stress detection using a micro-hyperspectral imager and a thermal camera," *Remote Sens. Environ.*, vol. 117, pp. 322–337, 2012.

[29] S. H. Caldwell, C. Kelleher, E. A. Baker, and L. K. Lautz, "Relative information from thermal infrared imagery via unoccupied aerial vehicle informs simulations and spatially-distributed assessments of stream temperature," *Sci. Total Environ.*, vol. 661, pp. 364–374, 2019.

[30] J. Miguel Costa, O.M. Grant, and M. Manuela Chaves, "Thermography to explore plant-environment interactions," *J. Exp. Botany*, vol. 64, no. 13, pp. 3937–3949, 2013.

[31] R. Calderon, J. A. Navas-Cortes, C. Lucena, and P. J. Zarco-Tejada, "High-resolution airborne hyperspectral and thermal imagery for early, detection of Verticillium wilt of olive using fluorescence, temperature and narrow-band spectral indices," *Remote Sens. Environ.*, vol. 139, pp. 231–245, 2013.

[32] J. Baluja *et al.*, "Assessment of vineyard water status variability by thermal and multispectral imagery using an unmanned aerial vehicle (UAV)," *Irrigation Sci.*, vol. 30, no. 6, pp. 511–522, 2012.

[33] C. Z. Espinoza, L. R. Khot, S. Sankaran, and P. W. Jacoby, "High resolution multispectral and thermal remote sensing-based water stress assessment in subsurface irrigated grapevines," *Remote Sens.*, vol. 9, no. 9, 2017, Art. no. 961.

[34] J. Bian *et al.*, "Simplified evaluation of cotton water stress using high resolution unmanned aerial vehicle thermal imagery," *Remote Sens.*, vol. 11, no. 3, 2019, Art. no. 267.

[35] V. Gonzalez-Dugo, P. Hernandez, I. Solis, and P. J. Zarco-Tejada, "Using high-resolution hyperspectral and thermal airborne imagery to assess physiological condition in the context of wheat phenotyping," *Remote Sens.*, vol. 7, no. 10, pp. 13586–13605, 2015.

[36] M. Smigaj, R. Gaulton, J. C. Suarez, and S. L. Barr, "Canopy temperature from an unmanned aerial vehicle as an indicator of tree stress associated with red band needle blight severity," *Forest Ecol. Manage.*, vol. 433, pp. 699–708, 2019.

[37] R. Calderon, J. A. Navas-Cortes, C. Lucena, and P. J. Zarco-Tejada, "High-resolution airborne hyperspectral and thermal imagery for early, detection of Verticillium wilt of olive using fluorescence, temperature and narrow-band spectral indices," *Remote Sens. Environ.*, vol. 139, pp. 231–245, 2013.

[38] J. Antonio Navarro, N. Algeet, A. Fernandez-Landa, J. Esteban, P. Rodriguez-Noriega, and M. Luz Guillen-Climent, "Integration of UAV, sentinel-1, and sentinel-2 data for mangrove plantation aboveground biomass monitoring in senegal," *Remote Sens.*, vol. 11, no. 77, pp. 77–100, 2019.

[39] D. W. Casbeer, D. B. Kingston, R. W. Beard, and T. W. McLain, "Cooperative forest fire surveillance using a team of small unmanned air vehicles," *Int. J. Syst. Sci.*, vol. 37, no. 6, pp. 351–360, 2006.

[40] M. C. Harvey, J. V. Rowland, and K. M. Luketina, "Drone with thermal infrared camera provides high resolution georeferenced imagery of the Waikite geothermal area, New Zealand," *J. Volcanol. Geothermal Res.*, vol. 325, pp. 61–69, 2016.

[41] A. I. Rahaghi, U. Lemmin, D. Sage, and D. A. Barry, "Achieving high-resolution thermal imagery in low-contrast lake surface waters by aerial remote sensing and image registration," *Remote Sens. Environ.*, vol. 221, pp. 773–783, 2019.

[42] F. Li, X. M. Cui, and G. T. Sun, "Approach of detecting coal fires by unmanned aerial vehicle thermal infrared remote sensing technology," *Saf. Coal Mines*, vol. 48, no. 12, pp. 97–100, 2017.

[43] M. D. Dios and A. Ollero, "Automatic detection of windows thermal heat losses in buildings using UAVs," in *Proc. World Autom. Congr.*. 2006, pp. 1–6.

[44] C. Webster, M. Westoby, N. Rutter, and T. Jonas, "Three-dimensional thermal characterization of forest canopies using UAV photogrammetry," *Remote Sens. Environ*, vol. 209, pp. 835–847, 2018.

[45] Z. Wu, Y. Wang, F. Kong, R. Sun, L. Chen, and W. Zhan, "Analysis of the thermal characteristics of selected urban surfaces in a typical residential area based on infrared thermography," *Acta Ecologica Sin.*, vol. 36, pp. 5421–5431, 2016.

[46] V. Sagan *et al.*, "UAV-based high resolution thermal imaging for vegetation monitoring, and plant phenotyping using ICI 8640 P, FLIR Vue Pro R 640, and thermoMap cameras," *Remote Sens.*, vol. 11, no. 3, 2019, Art. no. 330.

[47] J. A. Voogt and T. R. Oke, "Effects of urban surface geometry on remotely-sensed surface temperature," *Int. J. Remote Sens.*, vol. 19, no. 5, pp. 895–920, 1998.

[48] W. Bastiaanssen, "SEBAL-based sensible and latent heat fluxes in the irrigated Gediz Basin," *J. Hydrol.*, vol. 229, pp. 87–100, 2000.

[49] M. C. Anderson, J. M. Norman, W. P. Kustas, R. Houborg, P. J. Starks, and N. Agam, "A thermal-based remote sensing technique for routine mapping of land-surface carbon, water and energy fluxes from field to regional scales," *Remote Sens. Environ.*, vol. 112, no. 12, pp. 4227–4241, 2008.

[50] Y. Qin and J. E. Hiller, "Understanding pavement-surface energy balance and its implications on cool pavement development," *Energy Buildings*, vol. 85, pp. 389–399, 2014.

[51] D. P. Bentz, "A computer model to predict the surface temperature and time-of-wetness of concrete pavements and bridge decks," NIST, Gaithersburg, MD, USA, NIST Interagency/Internal Rep. (NISTIR) 6551, 2000,

[52] L. E. Landsberg, *The Urban Climate*. New York, NY, USA: Academic. 1981.

Li Feng received the B.S. degree in computer science and technology from Nanjing Normal University, Nanjing, China, in 2004, the M.S. degree in cartography and geographic information system from the School of Geographic and Oceanographic Sciences, Nanjing University, Nanjing, in 2007, and the Ph.D.degree in civil engineering from the Institute of Regional Development Planning, University Stuttgart, Stuttgart, Germany.

Currently, she is an Associate Professor with the School of Geographic Science and Engineering, Hohai University, Nanjing. From 2013 to 2015, she was a Postdoctoral Fellow with the Key Laboratory for Satellite Mapping Technology and Applications of State Administration of Surveying, Mapping, and Geoinformation of China, Nanjing University, Nanjing. During August 2018–January 2019, she was a Visiting Scholar with Boston University. Her research interests include remote sensing for urban vegetation quantity estimating and urban thermal environment.

Huihui Tian is currently working toward the master's degree in cartography and geography information system with the School of Geographic Science and Engineering, Hohai University, Nanjing, China.

Her research interests include urban thermal environment.

Zhi Qiao received the Ph.D. degree in environmental science from the School of Environment, Beijing Normal University, Beijing, China, in 2014.

He is currently a Lecturer with the School of Environmental Science and Engineering, Tianjin University, Tianjin, China. His current research interests include the applications of geographic information system and remote sensing on land-use and land-cover change and urban climate.

Menmen Zhao received the M.S. degree in cartography and geography information system from the School of Geographic Science and Engineering, Hohai University, Nanjing, China, in 2019.

Her research interests include urban thermal comfort.

Yanxia Liu is currently working toward the master's degree in cartography and geography information system with Hohai University, Nanjing, China.

Her current research interests include remote sensing application on land-use and land-cover change and urban vegetation phenology analysis.